

## Deep Metric Learning Based on Scalable Neighborhood Components for Remote Sensing Scene Characterization

Kang, J.; Fernandez-Beltran, R.; Ye, Z.; Tong, X.; Ghamisi, P.; Plaza, A.;

Originally published:

December 2020

**IEEE Transactions on Geoscience and Remote Sensing 58(2020)12, 8905-8918**

DOI: <https://doi.org/10.1109/TGRS.2020.2991657>

Perma-Link to Publication Repository of HZDR:

<https://www.hzdr.de/publications/Publ-31965>

Release of the secondary publication  
on the basis of the German Copyright Law § 38 Section 4.

# Deep Metric Learning based on Scalable Neighborhood Components for Remote Sensing Scene Characterization

Jian Kang, *Member, IEEE*, Ruben Fernandez-Beltran, Zhen Ye, Xiaohua Tong, *Senior Member, IEEE*, and Antonio Plaza, *Fellow, IEEE*

**Abstract**—With the development of convolutional neural networks (CNN), the semantic understanding of remote sensing scenes has been significantly improved based on their prominent feature encoding capabilities. Whereas many of the existing deep-learning models focus on designing different architectures, only few works in the remote sensing field have been addressed to investigate the performance of the learned feature embeddings and the associated metric space. In particular, two main loss functions have been exploited, the contrastive and the triplet loss. However, the straightforward application of these techniques for remote sensing images may not be optimal to capture their neighborhood structures in the metric space due to the insufficient sampling of image pairs or triplets during training and the inherent semantic complexity of the remotely sensed data. To solve these problems, we propose a novel deep metric learning approach for remote sensing, which overcomes the limitation on the class discrimination by means of two different components: 1) the scalable neighborhood component analysis loss, which targets for discovering the neighborhood structure in the metric space; and 2) the cross entropy loss, which aims at preserving the class discrimination capability based on the learned class prototype. Moreover, in order to preserve the feature consistency among all the mini-batches during training, a novel optimization mechanism based on momentum update is introduced for minimizing the proposed loss. An extensive experimental comparison, using several state-of-the-art models and two different benchmark datasets, has been conducted to validate the effectiveness of the proposed method from different perspectives, including 1) classification; 2) clustering; and 3) image retrieval. The related codes of this paper will be made publicly available for reproducible research inside the community.

**Index Terms**—Deep learning, metric learning, remote sensing scene characterization, dimensionality reduction.

This work has been supported by the Spanish Ministry of Economy (RTI2018-098651-B-C54), Junta de Extremadura (Ref. GR18060) and the European Union under the H2020 EOXP0SURE project (No. 734541). This work was supported in part by the National Key Research and Development Project of China under Grant 2018YFB0505400 and 2017YFB0502700, in part by the National Natural Science Foundation of China under Grant 41631178. (*Corresponding author: Zhen Ye*)

J. Kang is with the Department of Computer Engineering and Microelectronics, Technische Universität Berlin, 10587 Berlin, Germany (e-mail: jian.kang@tu-berlin.de).

R. Fernandez-Beltran is with the Institute of New Imaging Technologies, University Jaume I, 12071 Castellón de la Plana, Spain (e-mail: rufernan@uji.es).

Z. Ye and X. Tong are with College of Surveying and Geo-Informatics, Tongji University, 200092 Shanghai, China. (e-mail: yezhen0402@126.com; xhtong@tongji.edu.cn).

A. Plaza is with the Hyperspectral Computing Laboratory, Department of Technology of Computers and Communications, Escuela Politécnica, University of Extremadura, 10003 Cáceres, Spain. (e-mail: aplaza@unex.es).

## I. INTRODUCTION

WITH the ongoing development of different Earth Observation missions and programmes, the semantic understanding of remote sensing (RS) image scenes plays a fundamental role in many important applications and societal needs [1], including natural resources conservation [2], urban and regional planning [3], contingency management [4] and global Earth monitoring [5] among others. From a practical perspective, the RS scene recognition problem consists in predicting the semantic concept associated to a given aerial scene, based on its own visual content. In this way, scene-based recognition methods are expected to deal with high intra-class and low inter-class variabilities since airborne and space optical data often contain a wide variety of spatial structures that lead to a particularly challenging characterization for RS scenes [6].

In the literature, extensive research work has been conducted and several papers review the most relevant scene recognition methods within the RS field [7], [8]. Broadly speaking, three different trends can be identified when characterizing remotely sensed scenes: (1) low-level feature-based techniques; (2) unsupervised approaches; and (3) deep-learning methods. The former group of techniques is focused on extracting primary features from the input images using for that purpose straightforward visual descriptors such as color, texture, spectral-spatial shapes and also their combinations. From the simplest low-level feature-based approaches, which make use of color histograms [9], [10], to the most elaborated techniques, that consider texture features as well as gradient shape descriptors [11]–[13], all these methods have limitations when dealing with high-level semantic concepts due to the inherent complexity of the RS image domain [14].

In order to enhance the visual characterization and generalization, unsupervised feature learning approaches have been proposed to classify airborne and space optical data. The rationale behind this kind of methods is based on encoding the low-level features of the input scene into a higher-level feature space by means of unsupervised learning protocols. For instance, sparse coding [15], [16], topic modeling [17], [18] and auto-encoders [19], [20] are some of the most recent unsupervised paradigms that have been successfully applied to the RS field. Despite the fact that these and other methods are able to provide performance advantages with respect to traditional low-level feature-based techniques, the unsupervised

perspective of the encoding procedure may eventually reduce the intra-class discrimination ability, since actual scene classes are not taken into account.

Recently, deep-learning methods have attracted the RS research community attention due to their great potential to uncover highly discriminating features in aerial scenes [21]. More specifically, these approaches aim at projecting the input data onto the corresponding semantic label space through a hierarchy of nonlinear mappings and layers, which generate a high-level data characterization useful to classify remotely sensed imagery. For instance, Yao *et al.* propose in [22] a stacked sparse auto-encoder to extract deep features to effectively classify aerial images. With the increasing popularity of CNNs, other authors advocate the use of more complex deep-learning architectures (e.g., AlexNet [23], VGGNet [24] and GoogleNet [25]) to characterize and classify RS scenes. It is the case of Hu *et al.* who present in [26] two different scenarios to make use of VGGNet: (i) one directly using the last fully connected layers as image descriptors; and (ii) the other considering an encoding procedure over the last convolutional layer feature maps. Chaib *et al.* also present in [27] a RS classification method that employs the VGGNet model as feature extractor mechanism. Specifically, the authors adopt a feature fusion strategy where each layer is regarded as separated feature descriptors. Zang *et al.* define in [28] a deep ensemble framework based on gradient boosting which effectively combines several CNN-based characterizations. Analogously, Li *et al.* propose in [29] a multi-layer feature fusion framework which takes advantage of multiple pre-trained CNN models for RS scene classification. For the fine-grained land-use classification, Kang *et al.* exploit multiple CNN models to categorize different types of buildings based on street view images [30].

Despite the effectiveness achieved by these and other relevant methods in the literature [31], multiple research works highlight the benefits of using deep-learning embeddings to characterize aerial scenes [32]. In general, the so-called deep metric learning approach aims at projecting semantically similar input data to nearby locations in the final feature space by means of non-isotropic metrics [33]. As a result, it becomes a highly recommended scheme to simplify complex topological spaces which is often the case in the RS field. The unprecedented availability of airborne and space optical data together with the constant development of the acquisition technology are substantially increasing the complexity of the RS data and consequently its visual interpretation [1]. In addition, the probability of encountering unseen target scenes increases with the data complexity which also makes the embedding strategy appropriate for transferring the knowledge from the training samples to broader semantic domains [34].

Several works in the most recent RS literature exemplify these facts. For instance, Gong *et al.* adopt in [35] the Lifted Structured Feature Embedding approach ([36]) which defines a structured objective function based on the lifted pairwise distances within each training batch. The authors introduce an additional diversity-promoting criteria to decrease the metric parameter factor redundancy for RS scene classification. Cheng *et al.* present in [37] a simpler but effective

method to learn highly discriminative CNN-based features for aerial scenes. In particular, the authors impose a metric learning regularization term on the CNN features by means of the contrastive embedding scheme [38] which intrinsically enforces the model to be more discriminative and to achieve a competitive performance. Similarly, Yan *et al.* propose in [39] a cross-domain extension which aims at reducing the feature distribution bias and spectral shift in aerial shots considering a limited amount of target samples. Whether the model is created using network ensembles ([28]) or more elaborated semantic embeddings ([35], [37]), the special particularities of the RS domain still raise some important challenges when classifying aerial scenes [8]. The huge within-class diversity and between-class similarity within the RS field motivate the development of new operational processing chains to effectively learn discriminative CNN-based characterizations which pursue a better semantic generalization for unconstrained land cover scenes. Note that there are many factors, such as different sensing dates, instrument positions, lighting conditions and sensor types, that also affect remotely sensed data and hence its semantic understanding.

In order to face all these challenges, this paper proposes a novel RS scene characterization approach which provides a new perspective of the traditional deep embedding scheme typically used in land cover recognition tasks [35], [37]. The main objective of the proposed method consists in learning a low-dimensional metric space which can sufficiently capture the semantic similarities among all the RS scenes based on the CNN-based feature embedding of the whole data collection. Moreover, the learned feature embedding in such metric space has to be effectively generalized by means of the out-of-sample RS scenes. To achieve this goal, we first investigate the scalable neighborhood component analysis (SNCA) [40] and further analyze the limitations of this recent method on the discrimination of different RS scenes. Then, we develop an innovative deep metric learning approach which has been specifically designed to manage the particular semantic complexity of the RS image domain. Specifically, two main parts are involved in this novel design: 1) the SNCA loss, which targets for discovering the neighborhood structure in the metric space; and 2) the Cross Entropy (CE) loss, which aims at preserving the class discrimination capability based on the learned class prototypes. In addition, a novel optimization mechanism based on the momentum update for SNCA is proposed, in order to generate the consistent features within each training epoch. In order to demonstrate the effectiveness of our contribution when characterizing RS scenes, we conduct a comprehensive experimental comparison which reveals that our proposed RS scene characterization method provides competitive advantages with respect to different state-of-the-art models for three different RS applications (scene classification, clustering and retrieval) over two benchmark datasets. The main contributions of this paper can be summarized as follows:

- 1) To the best of our knowledge, this work investigates for the first time in the literature the suitability of using the SNCA method for characterizing remotely sensed image scenes while also analyzing its main limitations in RS.

- 2) We propose a new deep metric learning model specifically designed for characterizing RS scenes which is able to learn a metric space based on CNN models that preserves the discrimination capability for the highly variant RS semantic concepts.
- 3) In order to improve the consistency of the generated feature embeddings of the whole dataset during training, we propose a novel optimization mechanism based on momentum update for minimizing the SNCA-based losses.
- 4) Based on three different RS applications, the newly proposed method demonstrates its superiority with respect to several state-of-the-art characterization methods over different datasets. The related codes will be released for reproducible research inside the RS community.

The rest of this paper is organized as follows. Section II reviews some related works and highlights their main limitations to effectively characterize RS scenes. Section III presents the proposed deep metric learning model for RS. In Section IV, extensive experiments from different perspectives are conducted on several publicly available benchmark datasets. Finally, Section V concludes this paper and provides some remarks at plausible future research lines.

## II. RELATED WORK

### A. Deep Metric Learning

Deep metric learning methods aim to learn a low-dimensional metric space based on CNN models, where the feature embeddings of semantic-similar images should be close and those of dissimilar images should be separated. The metric space with such characteristics can be learned by applying proper loss functions. Most of the existing methods of deep metric learning can be categorized based on two types of loss functions [37], [41]–[43]: 1) the contrastive loss [38]; and 2) the triplet loss [44]. Some useful symbols and the definitions of these two losses are described as follows. Let  $\mathcal{X} = \{\mathbf{x}_1, \dots, \mathbf{x}_N\}$  define as a set of  $N$  RS images and  $\mathcal{Y} = \{\mathbf{y}_1, \dots, \mathbf{y}_N\}$  is the associated set of label vectors, where each label vector  $\mathbf{y}_i$  is represented by the one-hot vector i.e.,  $\mathbf{y}_i \in \{0, 1\}^C$ .  $C$  is the total number of classes. If the image is annotated by the class  $c$ , the  $c$ -th element of  $\mathbf{y}_i$  is 1, and 0 otherwise.  $\mathbf{v}_i \in \mathbb{R}^D$  denotes the feature of the  $i$ -th image  $\mathbf{x}_i$  obtained by a complex nonlinear mapping  $\mathcal{F}(\mathbf{x}_i; \theta)$  based on a CNN model, where the set  $\theta$  represents its learnable parameters.  $D$  is the dimension of the feature and  $\mathbf{f}_i$  is the normalized feature on the unit sphere (i.e.  $\mathbf{f}_i = \mathbf{v}_i / \|\mathbf{v}_i\|_2$ ). To train the deep metric learning system, a training set  $\mathcal{T}$  with  $M$  images are extracted from  $\mathcal{X}$ . According to this notation, the two aforementioned loss functions can be defined as:

#### 1) Contrastive Loss:

$$L_{\text{contrastive}} = \sum_{i,j} l_{ij} \|\mathbf{f}_i - \mathbf{f}_j\|_2^2 + (1 - l_{ij})h(m - \|\mathbf{f}_i - \mathbf{f}_j\|_2)^2, \quad (1)$$

where  $h(\cdot)$  represents the hinge loss function, i.e.,  $h(x) = \max(0, x)$ ,  $m$  is the predefined margin, and  $l_{ij}$  is the label indicator, satisfying:

$$l_{ij} = \begin{cases} 1, & \text{if } \mathbf{y}_i = \mathbf{y}_j, \\ 0, & \text{otherwise.} \end{cases} \quad (2)$$

Given an image pair  $(\mathbf{x}_i, \mathbf{x}_j)$  during training, the first term minimizes the Euclidean distance of the two feature embeddings if they share the same class, and the second term is minimized to separate their distance by a certain margin  $m$  if they belong to different classes.

#### 2) Triplet Loss:

$$L_{\text{triplet}} = \sum_i h(\|\mathbf{f}_i^a - \mathbf{f}_i^p\|_2^2 - \|\mathbf{f}_i^a - \mathbf{f}_i^n\|_2^2 + m), \quad (3)$$

where  $\mathbf{f}_i^a$ ,  $\mathbf{f}_i^p$  and  $\mathbf{f}_i^n$  are the feature embeddings of an anchor image  $\mathbf{x}_i^a$ , a positive image  $\mathbf{x}_i^p$ , and a negative image  $\mathbf{x}_i^n$ . Normally, the positive image shares the same class with the anchor image, and the class of the negative image is different with the anchor image. Given a triplet  $(\mathbf{f}_i^a, \mathbf{f}_i^p, \mathbf{f}_i^n)$ , triplet loss is minimized to push the negative image away from the anchor image so that their distance should be larger than the distance of the positive pair with a certain margin.

### B. Current Limitations in RS Scene Characterization

Most of the existing deep-learning based methods for RS scene characterization focus on developing different CNN architectures for improving the classification performance based on the semantic labels predicted by the CNN models. However, only few works in the RS field have been addressed to analyze the performance of the learned feature embeddings and the associated metric space. One of the pioneer works was proposed in [37] which introduces a novel loss function composed of the contrastive loss and the CE loss for learning discriminative feature from RS images. The contrastive loss is also exploited in [45] for encoding Synthetic Aperture Radar (SAR) scene images into low-dimensional features. In [46], a RS image retrieval method is proposed, which is based on the learned metric space by utilizing the triplet loss. Normally, the optimization of CNN models with respect to the contrastive or triplet loss functions is conducted stochastically with mini-batches. For the contrastive loss, negative and positive pairs are usually constructed for training the CNN models within each mini-batch. Nonetheless, this scheme has an important limitation when considering the inherent semantic complexity of the RS image domain. For example, we assume that each RS image can be seen once during one epoch of training and  $\mathbf{x}_i$  exists in one mini-batch for the current training iteration. The positive and negative images with respect to  $\mathbf{x}_i$  in this mini-batch can be only seen during the current iteration of training. However, CNN models cannot capture all the other positive and negative images with respect to  $\mathbf{x}_i$  outside the current mini-batch during this training epoch, which may lead to the insufficient learning of the network due to the particularly high intra-class and low inter-class variabilities of the RS images. For the triplet loss, one should build the whole set of possible triplets for training the CNN models and the number

of possible triplets is at the order of  $\mathcal{O}(|\mathcal{X}|^3)$  [47]. When considering a large-scale dataset, which is typically the case in RS, it will produce an unaffordable computational cost for sufficiently training the CNN models.

### III. PROPOSED DEEP METRIC LEARNING FOR RS

The proposed end-to-end deep metric learning model for RS scene characterization consists of three main parts. First, a backbone CNN architecture is considered in order to generate the corresponding feature embedding space for the input images. In this work, we make use of the ResNet [48] architecture due to its good performance to classify RS scenes [49]. Second, a new loss function, which contains a joint CE term and a SNCA term, is used to optimize the proposed model in order to address the challenges of within-class diversity and between-class similarity when characterizing RS scenes. Third, a novel optimization mechanism based on momentum update is proposed in order to better preserve the feature consistency within each training epoch than the memory-bank based mechanism proposed in [40]. Figure 1 provides a graphical illustration of the proposed deep metric learning approach. In the following sections, we describe in more detail the newly defined loss function and the considered optimization algorithm.

#### A. Loss Function

The SNCA [40] built upon the NCA [50], aims to find a metric space that can well preserve the neighborhood structure based on deep models with scalable datasets. Given a image pair  $(\mathbf{x}_i, \mathbf{x}_j)$  from the training set  $\mathcal{T}$ , their similarity  $s_{ij}$  in the metric space can be defined as cosine similarity:

$$s_{ij} = \mathbf{f}_i^T \mathbf{f}_j. \quad (4)$$

The image  $\mathbf{x}_i$  selects the image  $\mathbf{x}_j$  as its neighbor in the metric space with a probability  $p_{ij}$  as:

$$p_{ij} = \frac{\exp(s_{ij}/\sigma)}{\sum_{k \neq i} \exp(s_{ik}/\sigma)}, \quad p_{ii} = 0, \quad (5)$$

where  $\sigma$  is the temperature parameter controlling the concentration level of the sample distribution [51]. The higher similarity between  $\mathbf{x}_i$  and  $\mathbf{x}_j$ , there exists higher opportunity that  $\mathbf{x}_j$  can be selected as the neighbor of  $\mathbf{x}_i$  in the metric space than the other images  $\mathbf{x}_k$ .  $p_{ii} = 0$  indicates that each image cannot select itself as its neighbor. This probability is often termed as *leave-one-out* distribution on  $\mathcal{T}$ . Based on this, the probability that  $\mathbf{x}_i$  can be correctly classified is:

$$p_i = \sum_{j \in \Omega_i} p_{ij}, \quad (6)$$

where  $\Omega_i = \{j | \mathbf{y}_i = \mathbf{y}_j\}$  is the index set of training images sharing the same class with  $\mathbf{x}_i$ . Intuitively, the image  $\mathbf{x}_i$  can be correctly classified at a higher chance, if more images  $\mathbf{x}_j$  sharing the same class with  $\mathbf{x}_i$  are located as its neighbors in the metric space. The objective of SNCA is to minimize the expected negative log likelihood over  $\mathcal{T}$  with the definition:

$$L_{SNCA} = -\frac{1}{|\mathcal{T}|} \sum_i \log(p_i). \quad (7)$$

The gradient of  $L_{SNCA}$  with respect to  $\mathbf{f}_i$  is described as:

$$\frac{\partial L_{SNCA}}{\partial \mathbf{f}_i} = \frac{1}{\sigma} \sum_k p_{ik} \mathbf{f}_i - \frac{1}{\sigma} \sum_{k \in \Omega_i} \tilde{p}_{ik} \mathbf{f}_k, \quad (8)$$

where  $\tilde{p}_{ik} = p_{ik} / \sum_{j \in \Omega_i} p_{ij}$  is the normalized distribution of the ground-truth class. Based on the gradient in (8), the optimal solution of (7) will be reached, when the probability  $p_{ik}$  of negative images (i.e.  $k \notin \Omega_i$ ) equals to 0. In other words, the similarities between  $\mathbf{x}_i$  and some of positive images ( $k \in \Omega_i$ ) can also be very low in the metric space as long as there exist other positive images, which are the neighbors of  $\mathbf{x}_i$ . On the one hand, this characteristic can be beneficial to discover the inherent locality structure among the images in the metric space, especially there exist intra-class variations of the dataset. On the other hand, there is one limitation of SNCA for KNN classification. Since some of positive images ( $k \in \Omega_i$ ) do not have to be close to  $\mathbf{x}_i$ , their feature embeddings may be nearer to those of other negative images in the metric space. As illustrated in Figure 2a, the class A and B are separated and their intra-class variation can also be discovered, which is represented by the groups of light and dark points. However, given some out-of-sample images sharing similar features with some images from both classes, they cannot be correctly categorized by exploiting KNN classifier. One way to solve this problem is to separate the images from the two classes farther away from each other, which is illustrated in Figure 2b. With the same feature embeddings as in Figure 2a, the out-of-sample images are well recognized based on the KNN classifier. To achieve this goal, we introduce the CE loss for learning the class-wise prototype to align the images with respect to their associated classes.

The CE loss aims to measure the distance between the distribution of model outputs and the realistic distribution. In terms of the classification, the CE loss is defined as:

$$L_{CE} = -\frac{1}{|\mathcal{T}|} \sum_i \sum_c y_i^c \log(p_i^c), \quad (9)$$

where  $p_i^c$  denotes the probability that  $\mathbf{x}_i$  is classified into the class  $c$  formulated as:

$$p_i^c = \frac{\exp(\mathbf{w}_c^T \mathbf{v}_i)}{\sum_j \exp(\mathbf{w}_j^T \mathbf{v}_i)}, \quad (10)$$

where  $\mathbf{w}_c$  is the learned parameters of class  $c$ . Minimizing the CE loss (9) is to align all the images within the same class with the same vector  $\mathbf{w}_c$ . In that case, images from different classes are separated.

To this end, by taking advantages of the two losses, we propose a novel joint loss function for learning a low-dimensional metric space, which can preserve the neighborhood structure among the images and also distinguish the images from different classes. The proposed joint function, termed as *SNCA-CE* is defined as:

$$L = L_{CE} + \lambda L_{SNCA}, \quad (11)$$

where  $\lambda$  denotes the penalty parameter to control the balance between these two terms.

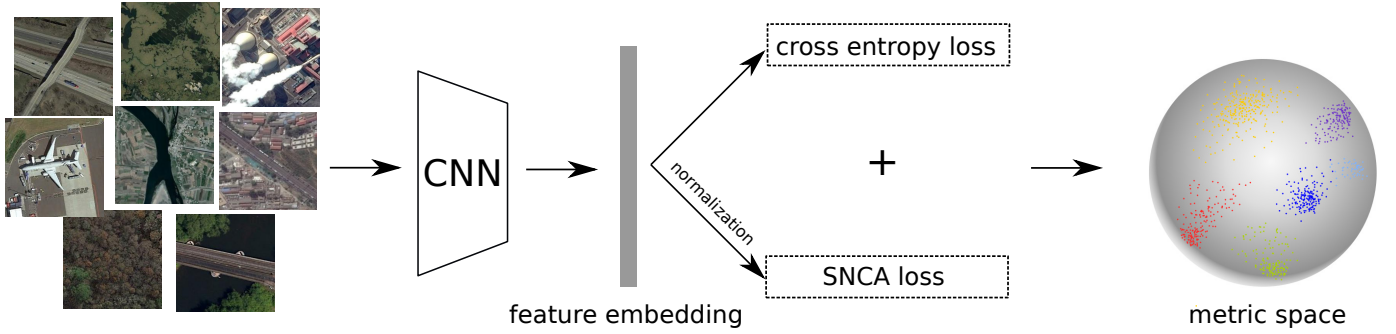


Fig. 1. Illustration of the proposed end-to-end deep metric learning model which is optimized using the newly defined loss function. By the proposed approach, we aim to encode the RS images into the learned metric space through a CNN model, where the intra-class feature embeddings are grouped together and inter-class feature embeddings are separated.

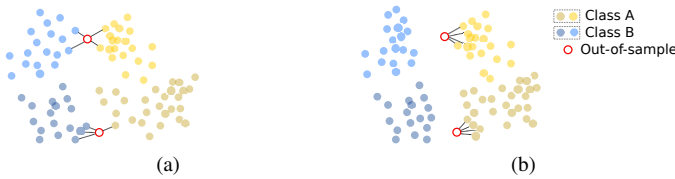


Fig. 2. Illustration of the limitation of the SNCA loss. (a) In the metric space produced by the SNCA loss, it will be challenging for KNN classifier to distinguish the out-of-sample images located near the border between the two classes. (b) By introducing CE loss, these two classes are further separated in the metric space, the same out-of-sample images in (a) can be accurately categorized based on KNN classifier.

### B. Optimization via Memory Bank

By applying the chain rule, we can obtain the gradient of the joint loss function with respect to  $\mathbf{f}_i$ :

$$\begin{aligned} \frac{\partial L_i}{\partial \mathbf{f}_i} = & -y_i^c(1-p_i^c)\|\mathbf{v}_i\|_2 \mathbf{w}_c + \frac{\lambda}{\sigma} \sum_k p_{ik} \mathbf{f}_k \\ & - \frac{\lambda}{\sigma} \sum_{k \in \Omega_i} \tilde{p}_{ik} \mathbf{f}_k. \end{aligned} \quad (12)$$

From (12), it can be observed that the feature embeddings of the entire dataset are needed for calculating the gradient. Following [40], we exploit a memory bank to store the normalized features, i.e.,  $\mathcal{B} = \{\mathbf{f}_1, \dots, \mathbf{f}_M\}$  and we suppose that these are up-to-date with the CNN parameters  $\theta$  trained at the  $t$ -th iteration, i.e.,  $\mathbf{f}_i^{(t)} \approx \mathcal{F}(\mathbf{x}_i; \theta^{(t)})/\|\mathbf{v}_i\|_2$ . At the  $(t+1)$ -th iteration, the gradient of the joint loss function with respect to  $\mathbf{f}_i$  is:

$$\begin{aligned} \frac{\partial L_i}{\partial \mathbf{f}_i} = & -y_i^c(1-p_i^c)\|\mathbf{v}_i^{(t)}\|_2 \mathbf{w}_c + \frac{\lambda}{\sigma} \sum_k p_{ik} \mathbf{f}_k^{(t)} \\ & - \frac{\lambda}{\sigma} \sum_{k \in \Omega_i} \tilde{p}_{ik} \mathbf{f}_k^{(t)}. \end{aligned} \quad (13)$$

Then,  $\theta$  can be learned by using the back-propagation technique, and  $\mathcal{B}$  can be updated by:

$$\mathbf{f}_i^{(t+1)} \leftarrow m \mathbf{f}_i^{(t)} + (1-m) \mathbf{f}_i, \quad (14)$$

where  $m$  is the parameter for the proximal regularization of  $\mathbf{f}_i$  based on its historical versions. We term this optimiza-

tion strategy as *SNCA-CE(MB)*. The associated optimization scheme is described in Algorithm 1.

---

#### Algorithm 1 SNCA-CE(MB)

---

**Require:**  $\mathbf{x}_i$ , and  $\mathbf{y}_i$

- 1: Initialize  $\theta$  and  $\mathcal{B}$  randomly,  $\sigma$ ,  $\lambda$ ,  $D$ ,  $m$
- 2: **for**  $t = 0$  to  $\text{maxEpoch}$  **do**
- 3:   Sample a mini-batch.
- 4:   Obtain  $\mathbf{f}_i^{(t)}$  and  $\mathbf{v}_i^{(t)}$  based on CNN with  $\theta^{(t)}$ .
- 5:   Calculate  $s_{ij}$  with reference to  $\mathcal{B}$ .
- 6:   Calculate the gradients based on (13).
- 7:   Back-propagate the gradients.
- 8:   Update  $\mathcal{B}$  via (14).
- 9: **end for**

**Ensure:**  $\theta$ ,  $\mathcal{B}$

---

### C. Optimization via Momentum Update

In SNCA-CE(MB), the features in  $\mathcal{B}$  is assumed up-to-date during training. However, this assumption cannot be easily satisfied, especially for scalable datasets. Suppose the image  $\mathbf{x}_i$  is observed in the first iteration of one training epoch and the associated feature  $\mathbf{f}_i^{(1)}$  generated by the CNN with the parameters  $\theta^{(1)}$  is stored in  $\mathcal{B}$ . Due to the training mechanism, this image cannot be observed again within the current epoch. Therefore, for the  $t$ -th iteration, the feature  $\mathbf{f}_j^{(t)}$  of image  $\mathbf{x}_j$  generated by the CNN with  $\theta^{(t)}$  is not consistent with  $\mathbf{f}_i^{(1)}$ , which is generated by a historical state of CNN. Since the optimization of SNCA-CE requires the look-up of the whole stored feature embeddings in  $\mathcal{B}$  for each iteration, such inconsistency may lead to a sub-optimal training of CNN.

To solve this issue, we propose a novel optimization mechanism based on momentum update [?] for the proposed SNCA-CE, termed as *SNCA-CE(MU)*. Instead of updating the feature embeddings stored in  $\mathcal{B}$ , the optimization scheme of SNCA-CE(MU) progressively updates the state of CNN in order to preserve the consistency of the features among all the mini-batches of each training epoch. To achieve this, an auxiliary CNN with the parameters  $\theta_{\text{aux}}$  is introduced, and  $\theta_{\text{aux}}$  is updated by:

$$\theta_{\text{aux}}^{(t+1)} \leftarrow m \theta_{\text{aux}}^{(t)} + (1-m) \theta^{(t)}, \quad (15)$$

where  $m \in [0, 1)$  is a momentum coefficient. It is worth noting that only the CNN with  $\theta$  is updated by back-propagation. The auxiliary CNN with the parameters  $\theta_{\text{aux}}$  can be evolved more smoothly than the CNN with  $\theta$ . To this end, the features in  $\mathcal{B}$  encoded by the auxiliary CNN are updated by:

$$\hat{\mathbf{f}}_i^{(t+1)} \leftarrow \hat{\mathbf{f}}_i^{(t)}, \quad (16)$$

where  $\hat{\mathbf{f}}_i$  denotes the generated features by the auxiliary CNN. In other words, the features in  $\mathcal{B}$  are replaced by the encoded features of the auxiliary CNN after each training epoch. The associated optimization scheme is described in Algorithm 2.

---

**Algorithm 2** SNCA-CE(MU)

---

**Require:**  $\mathbf{x}_i$ , and  $\mathbf{y}_i$

- 1: Initialize  $\theta$ ,  $\theta_{\text{aux}}$ , and  $\mathcal{B}$  randomly,  $\sigma$ ,  $\lambda$ ,  $D$ ,  $m$
- 2: **for**  $t = 0$  to  $\text{maxEpoch}$  **do**
- 3:   Sample a mini-batch.
- 4:   Obtain  $\mathbf{f}_i^{(t)}$  and  $\mathbf{v}_i^{(t)}$  based on CNN with  $\theta^{(t)}$ .
- 5:   Obtain  $\hat{\mathbf{f}}_i^{(t)}$  and  $\hat{\mathbf{v}}_i^{(t)}$  based on the auxiliary CNN with  $\theta_{\text{aux}}^{(t)}$ .
- 6:   Calculate  $s_{ij}$  based on  $\mathbf{f}_i^{(t)}$  and  $\mathcal{B}$ .
- 7:   Calculate the gradients based on (13).
- 8:   Back-propagate the gradients of  $\theta$ .
- 9:   Update the parameters  $\theta_{\text{aux}}$  of the auxiliary CNN via (15).
- 10:   Update  $\mathcal{B}$  via (16).
- 11: **end for**

**Ensure:**  $\theta$

---

## IV. EXPERIMENTS

### A. Dataset Description

In this work, two challenging RS image datasets have been used to validate the effectiveness of the proposed methods. Following, we provide a detailed description of the considered datasets:

- 1) **Aerial Image Dataset (AID)** [52]: This dataset is an important image collection which has been specially designed for aerial scene classification and retrieval. In particular, it is made of 10 000 RGB images belonging to the following 30 RS scene classes: airport, bare land, baseball field, beach, bridge, center, church, commercial, dense residential, desert, farmland, forest, industrial, meadow, medium residential, mountain, park, parking, playground, pond, port, railway station, resort, river, school, sparse residential, square, stadium, storage tanks and viaduct. Figure 3a illustrates some example scenes of this dataset. All the images are RGB acquisitions with a  $600 \times 600$  size. In addition, the number of images per class ranges from 220 to 420 and the spatial resolution also varies from 8 m to 0.5 m. The AID dataset is publicly available<sup>1</sup>.
- 2) **NWPU-RESISC45** [8]: This dataset is a large-scale RS dataset which contains 31 500 images uniformly

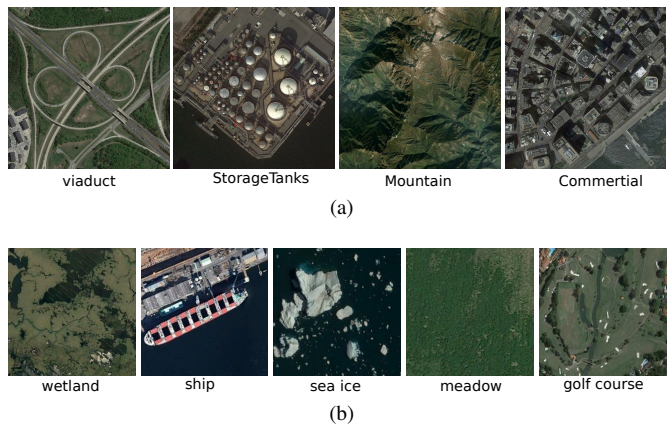


Fig. 3. Some sample images from the two benchmark datasets: (a) AID; and (b) NWPU-RESISC45.

distributed in 45 scene types: airplane, airport, baseball diamond, basketball court, beach, bridge, chaparral, church, circular farmland, cloud, commercial area, dense residential, desert, forest, freeway, golf course, ground track field, harbor, industrial area, intersection, island, lake, meadow, medium residential, mobile home park, mountain, overpass, palace, parking lot, railway station, rectangular farmland, river, roundabout, runway, sea ice, ship, snow-berg, sparse residential, stadium, storage tank, tennis court, terrace, thermal power station and wetland. Figure 3b shows some sample scenes of this dataset. All these aerial images are RGB shots with a  $256 \times 256$  size and a spatial resolution ranging from 30 m to 0.2 m. This dataset is also publicly available<sup>2</sup>.

### B. Experimental Setup

In order to extensively evaluate the effectiveness of the proposed method, we carry out several experiments from different perspectives, including: 1) image classification based on KNN classifier; 2) clustering; and 3) image retrieval.

1) *KNN Classification*: Given an out-of-sample image  $\mathbf{x}^*$ , its feature embedding  $\mathbf{f}^*$  is obtained by applying  $\mathcal{F}(\cdot)$  with the learned parameter set  $\theta$ . Based on the Euclidean distance between  $\mathbf{f}^*$  and the other stored embeddings in  $\mathcal{B}$ , we can get the top  $K$  nearest neighbors, and the predicted class  $\mathbf{y}^*$  can be determined based on their classes via majority voting. To evaluate the performance, we exploit the metrics of overall accuracy and class-wise F1 score.

2) *Clustering*: With the provided set of out-of-sample images, we can generate their feature embeddings based on  $\mathcal{F}(\cdot)$ . Their qualities can be assessed by applying a clustering task, such as K-means clustering. If the intra-class features are close and the inter-class features are separated in the metric space, they can be well clustered and the clustered labels can accurately match the ground-truth semantic labels. For the evaluation of clustering performance, the first measure we used is Normalized Mutual Information (NMI) [53], which is defined as:

$$\text{NMI} = \frac{2 \times I(\mathbf{Y}; \mathbf{C})}{H(\mathbf{Y}) + H(\mathbf{C})}, \quad (17)$$

<sup>1</sup>AID dataset : <http://goo.gl/WrJhu6>

<sup>2</sup>NWPU-RESISC45 dataset: <http://goo.gl/7YmQpK>

where  $\mathbf{Y}$  is the ground-truth class labels, and  $\mathbf{C}$  denotes the cluster labels based on the clustering method.  $I(\cdot; \cdot)$  and  $H(\cdot)$  represent the mutual information and entropy function, respectively. This metric measures the agreement of the ground-truth labels and the assigned labels based on the clustering method. We also calculate the unsupervised clustering accuracy as the second metric, formulated by:

$$\text{ACC} = \max_{\mathcal{M}} \frac{\sum_{i=1}^N \delta(l_i = \mathcal{M}(c_i))}{N}, \quad (18)$$

where  $l_i$  denotes the ground-truth class,  $c_i$  is the assigned cluster of image  $\mathbf{x}_i$ ,  $\delta(\cdot)$  represents the Dirac delta function.  $\mathcal{M}$  is the mapping function, which finds the best mapping between the cluster assigned labels with the ground-truth labels.

3) *Image Retrieval*: Image retrieval aims to find the most semantic-similar images in the archive based on their distances with respect to the query images. Such distance is measured through the similarities of the feature embeddings between the query images and the images of the archive in the metric space. Given the query image, more relevant images can be retrieved based on the feature embeddings generated by a more effective metric learning method. To evaluate the performance of image retrieval, we exploit the Precision-Recall (PR) curve to demonstrate the precision and recall metrics with respect to the varying number of retrieved images.

For these tasks, we randomly select 70% for training, 10% for validation and 20% for testing from the benchmark datasets. The clustering task is conducted on the feature embeddings of the test sets generated by the learned CNN model. For image retrieval, the test set is served for querying, and the training set is the archive. The proposed method is implemented in PyTorch [54]. The backbone CNN architecture is selected as ResNet18 [48]. The images are all resized to the size of  $256 \times 256$  and three data augmentation methods are adopted during training, which are: 1) *RandomGrayscale*, 2) *ColorJitter*, and 3) *RandomHorizontalFlip*. The parameters  $D$ ,  $\sigma$ ,  $\lambda$  and  $m$  are set as 128, 0.1, 1.0 and 0.5, respectively. Stochastic Gradient Descent (SGD) optimizer is employed for training. The initial learning rate is set to 0.01, and it is decayed by 0.5 every 30 epochs. The batch size is 256 and we totally train the CNN model for 100 epochs. To validate the effectiveness of the proposed method, we select several state-of-the-art methods of deep metric learning as the baseline, including: 1) D-CNN [37]. 2) deep metric learning based on triplet loss [44], [46], termed as Triplet and 3) SNCA(MB) [40]. It is worth noting that the original SNCA algorithm is optimized with memory bank, i.e. SNCA(MB). In order to validate the effectiveness of the proposed optimization mechanism, we also propose SNCA(MU) and compare its performance with the original SNCA[40]. For the triplet loss, the margin parameter is selected as 0.2 and the parameters in D-CNN are set the same as in the paper. All the experiments are conducted on a NVIDIA Tesla P100 GPU.

### C. Experimental Results

1) *KNN Classification*: Figure 4 demonstrates the learning curves of different methods with respect to the number of

training epochs based on the KNN classification results on the validation set of NWPU-RESISC45 when  $K = 10$ . To achieve an accuracy of 90%, SNCA(MU), SNCA-CE(MB) and SNCA-CE(MU) require less than 20 epochs, while the other methods take more than 20 epochs. As the learning curves converge, SNCA(MU), SNCA-CE(MB) and SNCA-CE(MU) can reach an accuracy with about 94%, which is around 2% higher than the others. Among them, the performances of SNCA-CE(MB) and SNCA-CE(MU) are slightly better than SNCA(MU) and SNCA-CE(MU) can achieve the fastest learning speed. By comparing SNCA-CE<sup>3</sup> with SNCA, the introduction of the CE loss can not only increase the learning speed, but also improve the classification accuracy in terms of the KNN classifier. By comparing the optimization mechanisms of MB and MU, updating the state of the CNN model can demonstrate its performance superiority than updating the memory bank. We present the overall accuracy of all the methods on the test sets in Table I with various  $K$ . Consistently with the validation, SNCA-CE(MB) and SNCA-CE(MU) can achieve the best classification performance on the two benchmark datasets. Compared with SNCA-CE(MB), the classification accuracy of SNCA-CE(MU) is slightly higher on the NWPU-RESISC45 dataset, while it is slightly lower on the AID dataset. Since the MU optimization mechanism is targeted for preserving the feature consistency among all the mini-batches through each training epoch, its advantage over MB may be more obvious on a larger dataset, e.g., NWPU-RESISC45. For the AID dataset, there are not many mini-batches within one training epoch, e.g., around 28, when the batch size is 256. The obtained feature embeddings in  $\mathcal{B}$  may not vary severely within each training epoch. Thus, the associated performance is comparable with the MU mechanism. SNCA-CE can obtain more accurate performances with more than 1% improvement compared with SNCA and more than 2% than the other two methods. With the adoption of momentum update, SNCA(MU) can achieve an accuracy improvement with a score around 0.5% than SNCA(MB). Moreover, Table II and Table III show the class-wise F1 scores of the two datasets, respectively, when  $K = 10$ . For the AID dataset, the F1 score of SNCA-CE(MB) on *Resort* class can achieve more than 5% performance gain than the other methods. For the NWPU-RESISC45 dataset, we can see that the performances of most classes obtained by SNCA-CE are the best compared with the others. Figure 5a and Figure 5b illustrate the similarities of the feature embeddings generated by D-CNN, Triplet, SNCA(MB) and SNCA-CE(MB) on the test sets of the AID and NWPU-RESISC45 datasets, respectively. The similarity is measured by applying *cosine distance*, i.e.  $\mathbf{f}_i^* \mathbf{f}_j^*$ . As shown by the similarity matrices, higher color contrast between the diagonal blocks and the background demonstrates higher dissimilarity between the images from one class and those from the others in the metric space. In terms of cosine distance, both SNCA(MB) and SNCA-CE(MB) can achieve better performances than D-CNN and Triplet for distinguishing different classes in the metric space.

<sup>3</sup>For simplicity, SNCA-CE refers to both SNCA-CE(MB) and SNCA-CE(MU), and it is the same with SNCA.

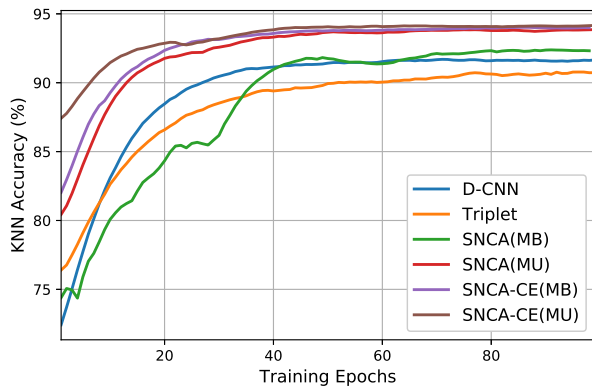


Fig. 4. Learning curves of different methods on the validation set with respect to number of training epochs. KNN accuracy (%) with  $K = 10$  at each epoch is recorded.

TABLE I  
KNN CLASSIFICATION OF DIFFERENT METHODS ON THE TEST SETS,  
WHEN  $K = 1, 5, 10$ .

	AID			NWPU-RESISC45		
	1	5	10	1	5	10
<b>D-CNN</b>	93.10	93.70	93.75	91.21	91.62	91.48
<b>Triplet</b>	92.85	93.10	93.25	90.83	91.46	91.43
<b>SNCA(MB)</b>	94.55	94.50	94.60	92.13	92.21	92.14
<b>SNCA(MU)</b>	94.55	94.75	94.75	92.57	92.59	92.68
<b>SNCA-CE(MB)</b>	<b>95.75</b>	<b>95.55</b>	<b>95.45</b>	93.84	93.84	93.79
<b>SNCA-CE(MU)</b>	95.15	95.40	95.15	<b>93.89</b>	<b>93.87</b>	<b>93.97</b>

2) *Clustering*: Table IV displays the NMI scores based on the K-means clustering applied on the feature embeddings of the test sets generated by all the methods. It can be observed that SNCA-CE can achieve the best matching between the ground-truth labels and the pseudo-labels assigned by K-means clustering, which provides more than 5% performance gain than D-CNN. Table V demonstrates the associated ACC scores obtained by all the methods. Consistent with NMI, the K-means clustering with the features generated by SNCA-CE

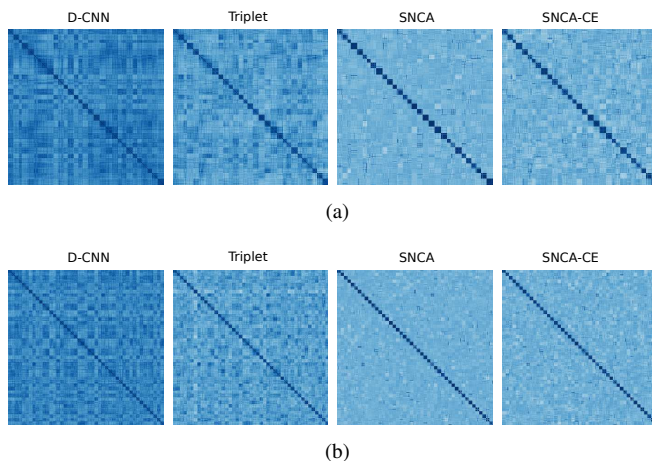


Fig. 5. Similarity matrices of the feature embeddings in the metric space obtained by different methods. The similarity is measured by cosine distance. (a) AID and (b) NWPU-RESISC45.

can make the best label assignment unsupervisedly. In order to get an insight of the feature embeddings in the metric space, we exploit t-distributed stochastic neighbour embedding (t-SNE) to visualize their projections in a 2D space. Figure 6 demonstrates the t-SNE scatter plots of the feature embeddings of the AID test set produced by: (a) D-CNN; (b) Triplet; and (c) SNCA-CE(MB). As illustrated in the results, the intra-class features are more compact and inter-class features are more isolated in the proposed method than the others. Therefore, in the metric space produced by the proposed method, clustering methods can more easily discover the inherent structure of the feature embeddings and the corresponding NMI score is higher than the other methods.

3) *Image Retrieval*: Figure 7 demonstrates the PR curves of the image retrieval results given the test set for querying, where Figure 7a and Figure 7b are the result on the AID, and NWPU-RESISC45 datasets, respectively. For a clear comparison, a zoom-in subplot is also displayed inside the figure. It can be seen that both SNCA and SNCA-CE show their superior performances over Triplet and D-CNN, as the number of retrieved images increases. As shown in the zoom-in subplots, the introduction of the CE loss can further improve the precision and recall performances based on the SNCA loss. For the SNCA-based methods (SNCA and SNCA-CE), the similarities of the images within one mini-batch during training are compared with all the other images in the dataset, so that the CNN model can be sufficiently optimized. As a comparison, for the contrastive loss utilized in D-CNN, the negative and positive image pairs are just sampled within each mini-batch. For other images outside this mini-batch, the corresponding negative and positive image pairs cannot be constructed, leading to the insufficient training of the CNN model. This is similar with respect to triplet loss. To make the CNN model capture the similarity and dissimilarity of all the images, one should make a triplet set with about  $\mathcal{O}(|\mathcal{T}|^3)$  triplets. It will be impossible for a scalable dataset. Such insufficiency of the trained CNN model based on the contrastive and triplet losses may induce that some images cannot be well separated against with other images from different classes or these images cannot be effectively grouped together with their relevant ones. This phenomenon can be observed in Figure 6, where some clusters shown in (a) and (b) are entangled with others. Additionally, this leads to the main factor that the performances of image retrieval based on SNCA and SNCA-CE are superior than the methods based on the contrastive and triplet losses. With respect to SNCA, by introducing the CE loss, SNCA-CE can further improve the image retrieval performance, owing to its enhanced class distinction capability. Figure 8 demonstrates some retrieved examples based on D-CNN, Triplet and the proposed method. Given two images from the two test sets, we present their top-5 nearest neighbors in the archive. As shown in Figure 8a, *Park* and *School* are confused with *Resort* in the result of Triplet on the AID dataset. For *freeway* in NWPU-RESISC45, it is confused with *overpass* by D-CNN as illustrated in Figure 8b.

4) *Parameter Sensitivity Analysis of SNCA-CE*: There are two main parameters in the proposed methods, i.e.,  $D$  and  $\sigma$ , where  $D$  determines the dimensionality of the feature embed-

TABLE II  
CLASS-WISE F1 SCORE OBTAINED BY THE KNN CLASSIFICATION OF DIFFERENT METHODS ON THE AID TEST SET, WHEN  $K = 10$ .

	D-CNN	Triplet	SNCA(MB)	SNCA(MU)	SNCA-CE(MB)	SNCA-CE(MU)
Airport	94.52	95.17	<b>97.18</b>	95.83	94.52	94.52
Bare Land	<b>95.93</b>	94.49	88.89	92.06	95.16	94.31
BaseballField	95.56	92.47	96.55	<b>97.73</b>	96.55	<b>97.73</b>
Beach	98.16	97.50	96.30	98.11	99.37	<b>100.00</b>
Bridge	95.77	97.18	<b>99.30</b>	98.61	<b>99.30</b>	97.90
Center	88.46	85.71	88.00	87.38	<b>89.11</b>	88.24
Church	88.66	88.17	94.85	<b>94.95</b>	87.38	93.07
Commercial	95.10	93.71	<b>96.50</b>	92.86	95.04	95.10
Dense Residential	93.33	94.55	98.18	96.34	<b>98.80</b>	96.93
Desert	96.61	93.33	91.67	95.73	<b>97.48</b>	<b>97.48</b>
Farmland	97.96	97.99	97.30	98.67	98.63	<b>99.32</b>
Forest	<b>100.00</b>	<b>100.00</b>	98.00	<b>100.00</b>	<b>100.00</b>	<b>100.00</b>
Industrial	<b>93.75</b>	92.31	91.61	92.81	92.50	93.51
Meadow	98.21	99.10	94.02	98.25	<b>99.12</b>	98.25
Medium Residential	94.83	92.04	<b>97.39</b>	94.12	<b>97.39</b>	94.21
Mountain	<b>100.00</b>	<b>100.00</b>	<b>100.00</b>	<b>100.00</b>	<b>100.00</b>	<b>100.00</b>
Park	82.99	83.33	85.92	87.14	<b>89.05</b>	<b>89.05</b>
Parking	<b>99.35</b>	<b>99.35</b>	98.09	<b>99.35</b>	98.72	98.72
Playground	92.81	92.00	96.73	97.33	95.42	<b>97.37</b>
Pond	97.01	97.04	95.91	97.04	96.55	<b>97.08</b>
Port	93.42	92.31	96.10	95.48	96.15	<b>97.44</b>
Railway Station	93.20	93.07	<b>95.41</b>	91.89	95.24	93.46
Resort	71.70	70.37	71.84	74.55	<b>81.48</b>	75.00
River	96.34	96.93	96.97	97.56	<b>99.39</b>	98.78
School	80.67	75.21	<b>84.75</b>	80.34	80.36	82.05
Sparse Residential	98.33	98.33	<b>99.16</b>	97.48	98.33	98.31
Square	83.33	85.27	89.23	89.39	<b>90.77</b>	85.48
Stadium	92.31	93.58	94.92	<b>97.35</b>	95.65	97.39
Storage Tanks	95.83	96.50	<b>97.26</b>	95.71	96.45	95.04
Viaduct	98.25	98.25	98.81	<b>99.41</b>	<b>99.41</b>	98.82

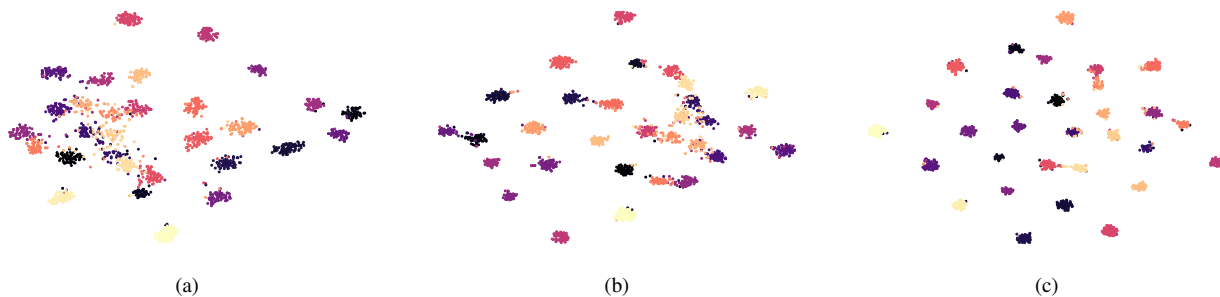


Fig. 6. 2D projection of the feature embeddings on the AID test set based on t-SNE: (a) D-CNN; (b) Triplet; and (c) SNCA-CE(MB).

dings in the metric space and  $\sigma$  controls the compactness of the sample distribution. Table VI demonstrates the effectiveness of the KNN classification based on SNCA-CE(MB) with respect to different  $D$  when  $K = 10$ . It can be seen that the classification performance is robust to  $D$  on both datasets. This characteristic will be beneficial for embedding large-scale datasets, since the features of small dimensionality can also maintain a high-quality classification performance. Based on the KNN classification when  $K = 10$ , we also report the effectiveness analysis based on SNCA-CE(MB) in terms of  $\sigma$  in Table VII. Within the range of 0.05 to 0.2, the classification results are stable. It indicates that for these two datasets, the

proposed method is insensitive with the choice of  $\sigma$  from 0.05 to 0.2.

## V. CONCLUSION

In this paper, we propose a novel deep metric learning approach for RS images which overcomes the limitation on scene discrimination by means of two different components: 1) the SNCA loss, which targets for constructing the neighborhood structure in the metric space; and 2) the CE loss, which aims at preserving the class discrimination capability. Moreover, to preserve the consistency among all the stored features during training, a novel optimization mechanism based on

TABLE III  
CLASS-WISE F1 SCORE OBTAINED BY THE KNN CLASSIFICATION OF DIFFERENT METHODS ON THE NWPU-RESISC45 TEST SET, WHEN  $K = 10$ .

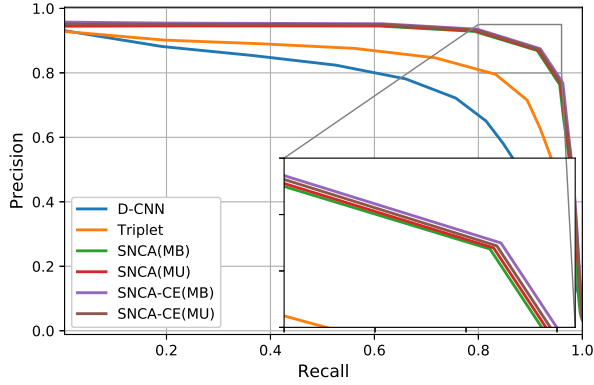
	D-CNN	Triplet	SNCA(MB)	SNCA(MU)	SNCA-CE(MB)	SNCA-CE(MU)
Airplane	96.82	96.86	98.22	98.57	<b>98.93</b>	98.23
Airport	91.84	92.15	88.32	92.14	<b>95.44</b>	95.41
Baseball diamond	95.00	94.58	97.12	<b>98.21</b>	96.45	96.09
Basketball court	92.59	92.94	96.77	96.80	<b>97.86</b>	97.16
Beach	94.62	96.77	96.35	96.75	97.16	<b>98.55</b>
Bridge	94.58	95.68	95.71	95.68	94.89	<b>96.73</b>
Chaparral	97.90	98.94	98.59	98.59	98.94	<b>99.29</b>
Church	72.46	71.33	74.26	76.47	<b>78.57</b>	76.12
Circular farmland	98.21	98.19	98.22	<b>99.64</b>	<b>99.64</b>	<b>99.64</b>
Cloud	<b>97.20</b>	96.55	94.85	96.50	<b>97.20</b>	96.55
Commercial area	85.22	81.12	87.32	85.11	<b>89.45</b>	88.81
Dense residential	88.00	87.63	87.59	88.81	90.97	<b>91.58</b>
Desert	91.51	93.43	92.68	94.37	94.16	<b>95.37</b>
Forest	94.48	93.52	93.52	95.80	<b>96.50</b>	96.14
Freeway	84.53	87.46	88.06	87.97	89.45	<b>91.58</b>
Golf course	95.68	96.38	97.51	95.68	<b>98.56</b>	98.23
Ground track field	96.17	96.73	96.84	97.16	98.23	<b>98.93</b>
Harbor	98.22	98.56	<b>98.92</b>	98.56	98.58	<b>98.92</b>
Industrial area	85.02	85.51	85.71	86.11	<b>87.77</b>	87.41
Intersection	88.36	92.68	91.17	94.66	94.08	<b>95.47</b>
Island	95.41	94.37	94.58	92.14	95.41	<b>95.77</b>
Lake	90.78	92.25	88.81	88.44	91.53	<b>92.73</b>
Meadow	91.45	90.39	91.76	92.09	<b>94.93</b>	94.24
Medium residential	86.11	83.33	83.92	84.10	<b>86.43</b>	86.33
Mobile home park	93.57	92.25	<b>96.14</b>	95.00	95.77	96.11
Mountain	88.05	91.29	90.34	92.86	92.68	<b>93.29</b>
Overpass	93.62	92.58	94.58	91.17	92.53	<b>93.91</b>
Palace	72.66	67.18	71.59	73.19	<b>75.18</b>	73.19
Parking lot	94.44	95.71	95.74	96.80	96.03	<b>97.84</b>
Railway	85.31	81.94	90.03	90.66	91.61	<b>92.36</b>
Railway station	86.93	83.87	84.59	<b>91.43</b>	88.17	90.00
Rectangular farmland	90.32	89.21	90.65	87.77	91.10	<b>91.58</b>
River	88.89	90.04	88.57	90.11	92.36	<b>93.48</b>
Roundabout	95.24	95.00	95.07	94.77	96.11	<b>96.14</b>
Runway	90.97	91.58	90.18	93.43	93.86	<b>94.16</b>
Sea ice	97.83	97.10	97.45	97.47	<b>98.55</b>	97.06
Ship	92.81	94.44	95.41	93.57	<b>97.18</b>	95.07
Snowberg	96.00	96.00	96.70	97.12	<b>97.44</b>	97.10
Sparse residential	95.80	<b>96.03</b>	93.95	94.58	94.96	95.34
Stadium	95.71	93.75	95.68	95.37	95.71	<b>96.14</b>
Storage tank	95.65	95.68	96.77	97.51	<b>97.87</b>	<b>97.87</b>
Tennis court	90.91	92.91	96.82	<b>97.53</b>	96.45	96.80
Terrace	91.04	90.39	92.20	90.03	<b>93.01</b>	91.99
Thermal power station	90.44	91.91	90.71	91.18	93.04	<b>93.33</b>
Wetland	86.79	86.92	84.58	87.97	88.89	<b>89.14</b>

TABLE IV  
NMI SCORES OF THE FEATURE EMBEDDINGS OF THE TEST SETS  
PRODUCED BY DIFFERENT METHODS.

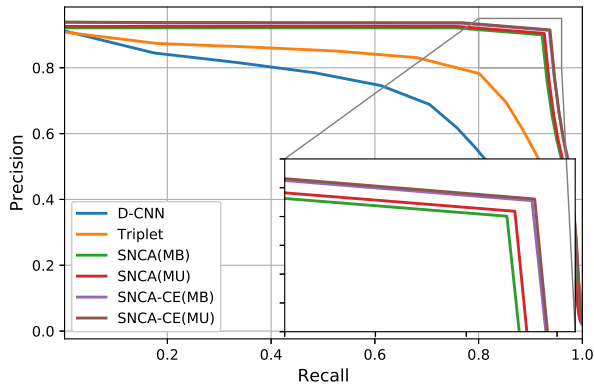
	AID	NWPU-RESISC45
D-CNN	88.83	85.30
Triplet	89.87	88.14
SNCA(MB)	92.96	90.20
SNCA(MU)	93.02	90.60
SNCA-CE(MB)	<b>93.98</b>	92.01
SNCA-CE(MU)	93.75	<b>92.28</b>

TABLE V  
ACC SCORES OF THE FEATURE EMBEDDINGS OF THE TEST SETS  
PRODUCED BY DIFFERENT METHODS.

	AID	NWPU-RESISC45
D-CNN	84.50	87.44
Triplet	92.50	88.33
SNCA(MB)	94.65	92.13
SNCA(MU)	94.80	91.22
SNCA-CE(MB)	<b>95.65</b>	93.71
SNCA-CE(MU)	95.25	<b>93.83</b>



(a)



(b)

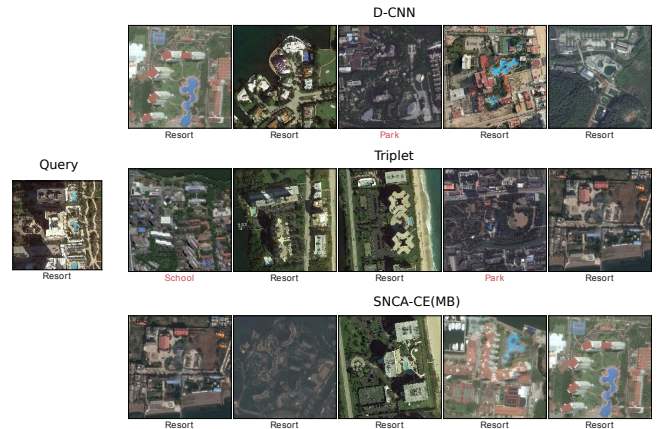
Fig. 7. PR curves of image retrieval results by different methods on the two datasets. The test sets are served for querying and the training sets are set as the archives. (a) AID and (b) NWPU-RESISC45.

TABLE VI  
SENSITIVITY ANALYSIS OF  $D$ .

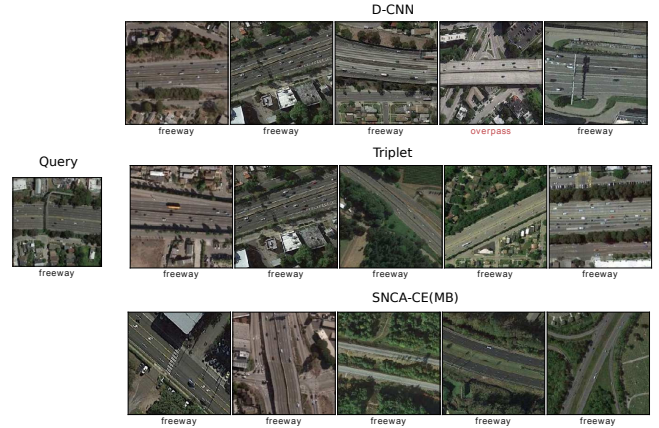
	AID	NWPU-RESISC45
$D = 32$	95.15	94.02
$D = 64$	95.60	94.13
$D = 128$	95.45	93.79

TABLE VII  
SENSITIVITY ANALYSIS OF  $\sigma$ .

	AID	NWPU-RESISC45
$\sigma = 0.05$	95.05	93.83
$\sigma = 0.1$	95.45	93.79
$\sigma = 0.15$	94.80	93.63
$\sigma = 0.2$	94.90	93.48



(a)



(b)

Fig. 8. Top-5 nearest neighbors retrieved with respect to the query images based on different methods. (a) AID and (b) NWPU-RESISC45.

momentum update is proposed for SNCA and SNCA-CE. To validate the effectiveness of the proposed method, we carry out extensive experiments from different perspectives, including 1) KNN classification; 2) clustering; and 3) image retrieval. These experiments demonstrate the superiority of the proposed methods over several state-of-the-art methods of deep metric learning, with the following advantages:

- Compared with contrastive and triplet losses, during training, the proposed loss can enforce the CNN model to "observe" all the negative and positive pairs associated to the images in each mini-batch by exploiting an offline memory bank. Thus, the CNN model can be sufficiently optimized for discovering the neighborhood structure in the metric space. Semantic-similar images can be better grouped than the methods based on contrastive and triplet losses.
- Compared with SNCA loss, the proposed SNCA-CE loss can further improve the class discrimination capability. Some images from different classes, which may be close in the metric space produced by SNCA, can be pushed away based on the learned category prototype in the CE loss.
- Through the optimization mechanism based on momentum update, the proposed SNCA(MU) demonstrates its

slight superiority based on the three tasks with respect to the original SNCA(MB) proposed in [40], and the performances of SNCA-CE(MB) and SNCA-CE(MU) are comparable. The MU optimization mechanism can ensure the smooth updating of the state of the CNN model. It will make the generated features of each mini-batch more consistent within one training epoch than those generated via the MB mechanism. Such characteristic can be more beneficial for processing a scalable dataset.

Besides the scene classification, the proposed deep metric learning method can be beneficial for different tasks in RS, e.g. dimensionality reduction of hyperspectral images and fine-grained land-use or land-cover classification. As a future work, we would like to investigate its capability for the scene classification with limited supervision.

## REFERENCES

- [1] Y. Ma, H. Wu, L. Wang, B. Huang, R. Ranjan, A. Zomaya, and W. Jie, "Remote sensing big data computing: Challenges and opportunities," *Future Generation Computer Systems*, vol. 51, pp. 47–60, 2015.
- [2] C. Corbane, S. Lang, K. Pipkins, S. Alleaume, M. Deshayes, V. E. G. Millán, T. Strasser, J. V. Borre, S. Toon, and F. Michael, "Remote sensing for mapping natural habitats and their conservation status—new opportunities and challenges," *International Journal of Applied Earth Observation and Geoinformation*, vol. 37, pp. 7–16, 2015.
- [3] Q. Weng, D. Quattrochi, and P. E. Gamba, *Urban remote sensing*. CRC press, 2018.
- [4] J. Li, Z. He, J. Plaza, S. Li, J. Chen, H. Wu, Y. Wang, and Y. Liu, "Social media: New perspectives to improve remote sensing for emergency response," *Proceedings of the IEEE*, vol. 105, no. 10, pp. 1900–1912, 2017.
- [5] N. Joshi, M. Baumann, A. Ehammer, R. Fensholt, K. Grogan, P. Hostert, M. R. Jepsen, T. Kuemmerle, P. Meyfroidt, E. T. Mitchard *et al.*, "A review of the application of optical and radar remote sensing data fusion to land use mapping and monitoring," *Remote Sensing*, vol. 8, no. 1, p. 70, 2016.
- [6] D. Bratasanu, I. Nedelcu, and M. Datcu, "Bridging the semantic gap for satellite image annotation and automatic mapping applications," *IEEE Journal of Selected Topics in Applied Earth Observations and Remote Sensing*, vol. 4, no. 1, p. 193, 2011.
- [7] C. Gómez, J. C. White, and M. A. Wulder, "Optical remotely sensed time series data for land cover classification: A review," *ISPRS Journal of Photogrammetry and Remote Sensing*, vol. 116, pp. 55–72, 2016.
- [8] G. Cheng, J. Han, and X. Lu, "Remote sensing image scene classification: Benchmark and state of the art," *Proceedings of the IEEE*, vol. 105, no. 10, pp. 1865–1883, 2017.
- [9] Y. Yang and S. Newsam, "Spatial pyramid co-occurrence for image classification," in *Computer Vision (ICCV), 2011 IEEE International Conference on*. IEEE, 2011, pp. 1465–1472.
- [10] G. Thoonen, Z. Mahmood, S. Peeters, and P. Scheunders, "Multisource classification of color and hyperspectral images using color attribute profiles and composite decision fusion," *IEEE Journal of Selected Topics in Applied Earth Observations and Remote Sensing*, vol. 5, no. 2, pp. 510–521, 2012.
- [11] Z. Li and L. Itti, "Saliency and gist features for target detection in satellite images," *IEEE Transactions on Image Processing*, vol. 20, no. 7, pp. 2017–2029, 2011.
- [12] E. Aptoula, "Remote sensing image retrieval with global morphological texture descriptors," *IEEE transactions on geoscience and remote sensing*, vol. 52, no. 5, pp. 3023–3034, 2014.
- [13] W. Zhang, X. Sun, K. Fu, C. Wang, and H. Wang, "Object detection in high-resolution remote sensing images using rotation invariant parts based model," *IEEE Geoscience and Remote Sensing Letters*, vol. 11, no. 1, pp. 74–78, 2014.
- [14] J. A. Benediktsson, J. Chanussot, and W. M. Moon, "Very high-resolution remote sensing: Challenges and opportunities [point of view]," *Proceedings of the IEEE*, vol. 100, no. 6, pp. 1907–1910, 2012.
- [15] A. M. Cheriyyadat, "Unsupervised feature learning for aerial scene classification," *IEEE Transactions on Geoscience and Remote Sensing*, vol. 52, no. 1, pp. 439–451, 2014.
- [16] M. L. Mekhalfi, F. Melgani, Y. Bazi, and N. Alajlan, "Land-use classification with compressive sensing multifeature fusion," *IEEE Geoscience and Remote Sensing Letters*, vol. 12, no. 10, pp. 2155–2159, 2015.
- [17] R. Fernandez-Beltran, J. M. Haut, M. E. Paoletti, J. Plaza, A. Plaza, and F. Pla, "Remote sensing image fusion using hierarchical multimodal probabilistic latent semantic analysis," *IEEE Journal of Selected Topics in Applied Earth Observations and Remote Sensing*, 2018.
- [18] R. Fernandez-Beltran and F. Pla, "Sparse multi-modal probabilistic latent semantic analysis for single-image super-resolution," *Signal Processing*, vol. 152, pp. 227–237, 2018.
- [19] E. Li, P. Du, A. Samat, Y. Meng, and M. Che, "Mid-level feature representation via sparse autoencoder for remotely sensed scene classification," *IEEE Journal of Selected Topics in Applied Earth Observations and Remote Sensing*, vol. 10, no. 3, pp. 1068–1081, 2017.
- [20] F. Lv, M. Han, and T. Qiu, "Remote sensing image classification based on ensemble extreme learning machine with stacked autoencoder," *IEEE Access*, vol. 5, pp. 9021–9031, 2017.
- [21] L. Zhang, L. Zhang, and B. Du, "Deep learning for remote sensing data: A technical tutorial on the state of the art," *IEEE Geoscience and Remote Sensing Magazine*, vol. 4, no. 2, pp. 22–40, 2016.
- [22] X. Yao, J. Han, G. Cheng, X. Qian, and L. Guo, "Semantic annotation of high-resolution satellite images via weakly supervised learning," *IEEE Transactions on Geoscience and Remote Sensing*, vol. 54, no. 6, pp. 3660–3671, 2016.
- [23] A. Krizhevsky, I. Sutskever, and G. E. Hinton, "Imagenet classification with deep convolutional neural networks," in *Advances in neural information processing systems*, 2012, pp. 1097–1105.
- [24] K. Simonyan and A. Zisserman, "Very deep convolutional networks for large-scale image recognition," *arXiv preprint arXiv:1409.1556*, 2014.
- [25] C. Szegedy, W. Liu, Y. Jia, P. Sermanet, S. Reed, D. Anguelov, D. Erhan, V. Vanhoucke, and A. Rabinovich, "Going deeper with convolutions," in *Proceedings of the IEEE conference on computer vision and pattern recognition*, 2015, pp. 1–9.
- [26] F. Hu, G.-S. Xia, J. Hu, and L. Zhang, "Transferring deep convolutional neural networks for the scene classification of high-resolution remote sensing imagery," *Remote Sensing*, vol. 7, no. 11, pp. 14 680–14 707, 2015.
- [27] S. Chaib, H. Liu, Y. Gu, and H. Yao, "Deep feature fusion for vhr remote sensing scene classification," *IEEE Trans. Geosci. Remote Sens.*, vol. 55, no. 8, pp. 4775–4784, 2017.
- [28] F. Zhang, B. Du, and L. Zhang, "Scene classification via a gradient boosting random convolutional network framework," *IEEE Transactions on Geoscience and Remote Sensing*, vol. 54, no. 3, pp. 1793–1802, 2016.
- [29] E. Li, J. Xia, P. Du, C. Lin, and A. Samat, "Integrating multilayer features of convolutional neural networks for remote sensing scene classification," *IEEE Transactions on Geoscience and Remote Sensing*, vol. 55, no. 10, pp. 5653–5665, 2017.
- [30] J. Kang, M. Körner, Y. Wang, H. Taubenböck, and X. X. Zhu, "Building instance classification using street view images," *ISPRS journal of photogrammetry and remote sensing*, vol. 145, pp. 44–59, 2018.
- [31] K. Nogueira, O. A. Penatti, and J. A. dos Santos, "Towards better exploiting convolutional neural networks for remote sensing scene classification," *Pattern Recognition*, vol. 61, pp. 539–556, 2017.
- [32] O. A. Penatti, K. Nogueira, and J. A. dos Santos, "Do deep features generalize from everyday objects to remote sensing and aerial scenes domains?" in *Proceedings of the IEEE conference on computer vision and pattern recognition workshops*, 2015, pp. 44–51.
- [33] J. Hu, J. Lu, and Y.-P. Tan, "Deep transfer metric learning," in *Proceedings of the IEEE Conference on Computer Vision and Pattern Recognition*, 2015, pp. 325–333.
- [34] A. Li, Z. Lu, L. Wang, T. Xiang, and J.-R. Wen, "Zero-shot scene classification for high spatial resolution remote sensing images," *IEEE Transactions on Geoscience and Remote Sensing*, vol. 55, no. 7, pp. 4157–4167, 2017.
- [35] Z. Gong, P. Zhong, Y. Yu, and W. Hu, "Diversity-promoting deep structural metric learning for remote sensing scene classification," *IEEE Transactions on Geoscience and Remote Sensing*, vol. 56, no. 1, pp. 371–390, 2018.
- [36] H. Oh Song, Y. Xiang, S. Jegelka, and S. Savarese, "Deep metric learning via lifted structured feature embedding," in *Proceedings of the IEEE Conference on Computer Vision and Pattern Recognition*, 2016, pp. 4004–4012.
- [37] G. Cheng, C. Yang, X. Yao, L. Guo, and J. Han, "When deep learning meets metric learning: Remote sensing image scene classification via learning discriminative cnns," *IEEE transactions on geoscience and remote sensing*, vol. 56, no. 5, pp. 2811–2821, 2018.

- [38] R. Hadsell, S. Chopra, and Y. LeCun, "Dimensionality reduction by learning an invariant mapping," in *2006 IEEE Computer Society Conference on Computer Vision and Pattern Recognition (CVPR'06)*, vol. 2. IEEE, 2006, pp. 1735–1742.
- [39] L. Yan, R. Zhu, N. Mo, and Y. Liu, "Cross-domain distance metric learning framework with limited target samples for scene classification of aerial images," *IEEE Transactions on Geoscience and Remote Sensing*, 2019.
- [40] Z. Wu, A. A. Efros, and S. X. Yu, "Improving generalization via scalable neighborhood component analysis," in *Proceedings of the European Conference on Computer Vision (ECCV)*, 2018, pp. 685–701.
- [41] Y. Tian, C. Chen, and M. Shah, "Cross-view image matching for geo-localization in urban environments," in *Proceedings of the IEEE Conference on Computer Vision and Pattern Recognition*, 2017, pp. 3608–3616.
- [42] G. Cheng, P. Zhou, and J. Han, "Duplex metric learning for image set classification," *IEEE Transactions on Image Processing*, vol. 27, no. 1, pp. 281–292, 2017.
- [43] J. Han, G. Cheng, Z. Li, and D. Zhang, "A unified metric learning-based framework for co-saliency detection," *IEEE Transactions on Circuits and Systems for Video Technology*, vol. 28, no. 10, pp. 2473–2483, 2017.
- [44] F. Schroff, D. Kalenichenko, and J. Philbin, "Facenet: A unified embedding for face recognition and clustering," in *Proceedings of the IEEE conference on computer vision and pattern recognition*, 2015, pp. 815–823.
- [45] J. Wang, P. Virtue, and S. X. Yu, "Successive embedding and classification loss for aerial image classification," *arXiv preprint arXiv:1712.01511*, 2017.
- [46] R. Cao, Q. Zhang, J. Zhu, Q. Li, Q. Li, B. Liu, and G. Qiu, "Enhancing remote sensing image retrieval with triplet deep metric learning network," *arXiv preprint arXiv:1902.05818*, 2019.
- [47] Y. Movshovitz-Attias, A. Toshev, T. K. Leung, S. Ioffe, and S. Singh, "No fuss distance metric learning using proxies," in *Proceedings of the IEEE International Conference on Computer Vision*, 2017, pp. 360–368.
- [48] K. He, X. Zhang, S. Ren, and J. Sun, "Deep residual learning for image recognition," in *Proceedings of the IEEE conference on computer vision and pattern recognition*, 2016, pp. 770–778.
- [49] S. Song, H. Yu, Z. Miao, Q. Zhang, Y. Lin, and S. Wang, "Domain adaptation for convolutional neural networks-based remote sensing scene classification," *IEEE Geoscience and Remote Sensing Letters*, vol. 16, no. 8, pp. 1324–1328, 2019.
- [50] J. Goldberger, G. E. Hinton, S. T. Roweis, and R. R. Salakhutdinov, "Neighbourhood components analysis," in *Advances in neural information processing systems*, 2005, pp. 513–520.
- [51] G. Hinton, O. Vinyals, and J. Dean, "Distilling the knowledge in a neural network," *arXiv preprint arXiv:1503.02531*, 2015.
- [52] G.-S. Xia, J. Hu, F. Hu, B. Shi, X. Bai, Y. Zhong, L. Zhang, and X. Lu, "Aid: A benchmark data set for performance evaluation of aerial scene classification," *IEEE Transactions on Geoscience and Remote Sensing*, vol. 55, no. 7, pp. 3965–3981, 2017.
- [53] H. Schütze, C. D. Manning, and P. Raghavan, "Introduction to information retrieval," in *Proceedings of the international communication of association for computing machinery conference*, 2008, p. 260.
- [54] A. Paszke, S. Gross, F. Massa, A. Lerer, J. Bradbury, G. Chanan, T. Killeen, Z. Lin, N. Gimelshein, L. Antiga *et al.*, "Pytorch: An imperative style, high-performance deep learning library," in *Advances in Neural Information Processing Systems*, 2019, pp. 8024–8035.